

# Novel Colloidal Silica Technology For *In Situ* Spinelization in MgO-Containing Refractories

Rafael Salomão<sup>a\*</sup>, Leandro Fernandes<sup>a</sup>, Andreas Sundblom<sup>b</sup>, Peter Greenwood<sup>b</sup>,

Isabela Santos Martinatti<sup>c</sup>, Paulo Roberto Teruo Tiba<sup>c</sup>

<sup>a</sup>Universidade de São Paulo, Escola de Engenharia de São Carlos, Departamento de Engenharia de Materiais, São Carlos, SP, Brasil.

<sup>b</sup>Nouryon AB, Göteborg, Sweden.

<sup>c</sup>Nouryon South America, Jundiaí, SP, Brasil.

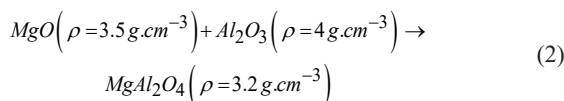
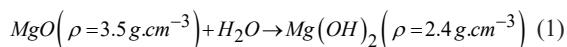
Received: October 04, 2023; Revised: January 30, 2024; Accepted: March 03, 2024

This study used an aqueous dispersion of silanized colloidal silica (SCS), whose particles' surfaces were modified with an epoxysilane-based coupling agent, as the liquid medium and binder for MgO-Al<sub>2</sub>O<sub>3</sub>-containing suspensions. Fine calcined alumina and magnesia sinter particles were dispersed in SCS to form a 65 vol% solids suspension. Equivalent silica-free compositions containing calcium aluminate cement or unsilanized colloidal silica were tested as references. After mixing, the SCS-suspension showed low viscosity and suitable workability and, after curing, a thin protective coating of magnesium silicate hydrate (MSH) was formed, thus preventing MgO hydroxylation and improving bonding strength, generating green-dried structures of significant flexural strength (8 MPa). During initial heating, the decomposition of MSH and the softening of amorphous silica particles reduced the overall expansion of spinel (MgAl<sub>2</sub>O<sub>4</sub>) formation. After sintering at 1600°C, the structure showed intense densification (total porosity of 8%) high flexural strength (73 MPa) and large spinel crystals surrounded by a thin layer of amorphous silica and magnesium silicates.

**Keywords:** *Magnesia sinter; in situ spinel, silanized colloidal silica.*

## 1. Introduction

Magnesium aluminate spinel (MgAl<sub>2</sub>O<sub>4</sub>) is a chief raw material for steelmaking due to its high refractoriness, corrosion resistance, and tolerance to thermal shock damages<sup>1-4</sup>. In monolithic refractories, it comprises pre-formed coarse aggregates, or can be formed *in situ* from fine sources of MgO and Al<sub>2</sub>O<sub>3</sub> for their matrix<sup>5-8</sup>. Despite such a energy-saving technological advantage, *in situ* spinel-containing monolithic refractories face two major drawbacks related to reactions that occur during their processing, namely a) hydroxylation of MgO during mixing, curing, and drying steps (Equation 1<sup>9-16</sup>), and b) *in situ* formation of spinel during sintering (Equation 2<sup>8,17-24</sup>).



In both cases, the density mismatch between initial reactants and the products formed results in highly expansive reactions capable of producing mechanical damages that vary from warping and microcracks up to the total crumbling of the structure and hindering densification<sup>8,19,20,25-30</sup>.

Over the past three decades, several solutions have been proposed towards hindering or at least minimizing the impact

of such drawbacks. Regarding MgO hydroxylation, they have aimed at determining the most relevant variables that affect the reaction<sup>9,12,14,31-38</sup> and developing hydroxylation-resistant raw materials<sup>10,11,13,15</sup>, anti-hydroxylation additives<sup>39-46</sup>, and strategies for using the volumetric expansion in a controlled binding effect<sup>47,48</sup>. Regarding *in situ* spinel, studies have investigated the role of particles' diameter distribution<sup>6,25,26,49</sup>, binders<sup>7,28</sup>, and other raw materials<sup>4,20,22,29</sup>, mineralizing agents<sup>3,27,50</sup>, and formation conditions<sup>4,21,24,51-63</sup>. Based on such findings, this study proposes a simultaneous solution for both drawbacks.

A recent paper from the authors' research group addressed the use of a novel grade of anionic silanized colloidal silica (SCS) dispersion as a liquid medium and binding agent for the production of concentrate suspensions of fine MgO sinter with excellent workability and hydroxylation resistance<sup>46</sup>. The surfaces of the colloidal silica particles were previously modified by an epoxysilane-based coupling agent for improving their stability and preventing instantaneous gelling (Figure 1a)<sup>64-66</sup>. During mixing, the negatively charged particles of SCS heterocoagulated over MgO surfaces containing positive charges to form a magnesium silicate hydroxide hydrate protective coating (Mg<sub>5</sub>Si<sub>8</sub>O<sub>20</sub>(OH)<sub>2</sub>·8H<sub>2</sub>O, Figure 1b)<sup>46</sup>. Its high stability halted the hydroxylation reaction and prevented the damage of volumetric expansion even under harsh hydroxylation tests, such as one-week-long curing steps and hydrothermal reactors (Figure 1c). After drying and as the initial heating proceeded, the protective coating favored early densification generating a small quantity of forsterite

\*e-mail: [rsalomao@sc.usp.br](mailto:rsalomao@sc.usp.br)

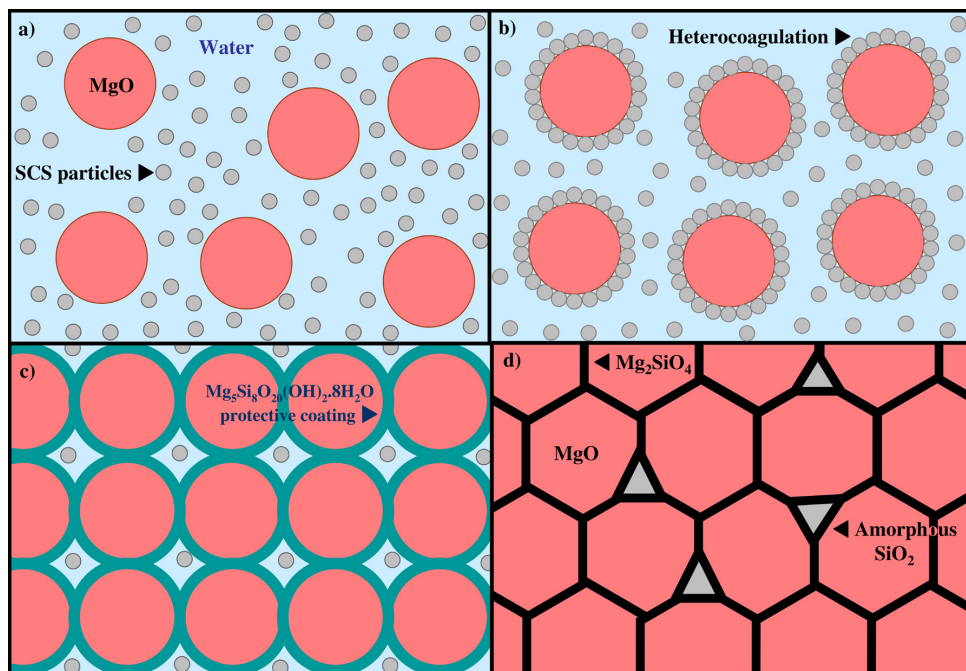


**Figure 1.** Schematic representation of the protective anti-hydroxylation-binding mechanism proposed in Salomão et al.<sup>46</sup> observed in MgO-silanized colloidal silica-containing dispersions: a-b) during mixing, c) curing, and d) after sintering.

( $\text{Mg}_2\text{SiO}_4$ , 2 wt%) and non-crystalline silica surrounding MgO grains (Figure 1d) after sintering.

Such promising results suggest the same strategy could be employed in a MgO- $\text{Al}_2\text{O}_3$  system for preventing hydroxylation damages. Moreover, the remaining amorphous silica content would help to reduce the effects of *in situ* spinel formation<sup>3,27,67</sup>, maintaining the benefits of the straightforward processing of colloidal silica-bonded castables<sup>2,5,68-74</sup>. This hypothesis was investigated in the present study in a composition prepared with calcined alumina, fine magnesia sinter, and silanized colloidal silica through flowability, drying and hydroxylation tests, and physical properties (total porosity, flexural strength, and thermal dimensional variations) and microstructure evolution (SEM and XDR) during the initial heating towards sintering. Equivalent compositions prepared with calcium aluminate cement and water or unsilanized anionic colloidal silica were also tested under the same parameters as references.

## 2. Experimental

### 2.1. Raw material characterization, mixing, and flowability tests

Raw materials: Calcined alumina (CA,  $\alpha\text{-Al}_2\text{O}_3$ , E-sy 1000, Almatix, USA), magnesia sinter (MS,  $\alpha\text{-MgO}$ , High-Purity M30, Magnesita-RHI, Brazil), calcium aluminate cement (CAC, 67 wt%  $\text{Al}_2\text{O}_3$ , EL70, ELFUSA Geral de Eletrofusão, Brazil), unsilanized colloidal silica (UCS, Levasil CS40-222), silanized colloidal silica (SCS, FX401, Nouryon AB, Sweden), water ( $\text{H}_2\text{O}$ , double distilled), dispersant (poly(ethylene glycol)-based, Castment FS-20, BASF, Germany). Particles' characterization: chemical

composition (X-ray dispersive spectroscopy, Shimadzu, EDX 720, Japan, after calcination at  $1000^\circ\text{C}$  for 5 h); crystalline phases' composition (X-ray diffraction, Rotaflex RV 200B, Rigaku-Denki Corp., Japan,  $\lambda = 0.14506$  nm, in the  $2\theta$  range from  $10$  to  $70^\circ$  at a  $0.5^\circ\cdot\text{min}^{-1}$  scan rate, against standard JCPDS files); particles' diameter distribution (acoustic emission method, DT-1202, Dispersion Technology Inc., USA), solid density (Helium pycnometry, Ultrapyc 1200e, Quantachrome Instruments, USA); specific surface area (high-purity  $\text{N}_2$  adsorption, BET method, Nova 1200e, Quantachrome Instruments, USA, ASTM C 1069-09 "Standard Test Method for Specific Surface Area of Alumina or Quartz by Nitrogen Adsorption"); moisture and water content (Thermogravimetric analysis, TGA-Q50, TA Instruments, 25- $1000^\circ\text{C}$ , synthetic air atmosphere) (Table 1).

The dried raw materials were previously dry-mixed and then mixed with water (CA-MS-CAC formulation), unsilanized colloidal silica dispersion (CA-MS-UCS formulation), or silanized colloidal silica dispersion (CA-MS-SCS formulation) (Table 1), and homogenized as suspensions in a paddle mixer (PowerVisc, IKA, Germany, 1000 rpm, 3 min). The CAC-containing composition was tested as reference because it is the most used and studied binder in MgO-containing monolithic refractories<sup>2,42</sup>; the UCS-containing one, on the other hand, demonstrates the deleterious effects of the instantaneous gelling of colloidal silica in presence of large quantity of  $\text{Mg}^{2+}$  ions<sup>69-71</sup>. It is also important to highlight two aspects. Firstly, no coarse aggregates were added to the compositions to allow a more accurate study of the reactions involved and the products formed. Secondly, the amounts of CaO and  $\text{SiO}_2$  from calcium aluminate cement and colloidal silica, respectively, at the compositions during sintering is similar or lower than the

**Table 1.** Characteristics of the raw materials employed and formulations tested.

| Raw materials' characteristics                               | Calcined alumina (CA)                             | MgO sinter (MS)        | Calcium aluminate cement (CAC)  | Unsilanized colloidal silica (UCS) | Silanized colloidal silica (SCS) |        |
|--|---|------------------------|---|------------------------------------|----------------------------------|--------|
| <sup>a</sup> Composition (wt%)                               | Al <sub>2</sub> O <sub>3</sub>                    | 99.4                   | 0.09  | 67.4                               | -                                | -      |
|  | MgO   | 0.03                   | 99.1  | 0.34                               | -                                | -      |
|  | SiO <sub>2</sub>                                  | 0.31                   | 0.18  | 3.60                               | 99.95                            | 99.95  |
|  | Na <sub>2</sub> O                                 | 0.20                   | 0.16  | 0.13                               | < 0.05                           | < 0.05 |
|  | Fe <sub>2</sub> O <sub>3</sub>                    | 0.03                   | 0.15  | 0.43                               | -                                | -      |
|  | CaO   | 0.03                   | 0.32  | 28.1                               | -                                | -      |
| <sup>b</sup> Crystalline phases (PDF file)                   | $\alpha$ -Al <sub>2</sub> O <sub>3</sub> (1-1243) | $\alpha$ -MgO (1-1235) | 68% CaAl <sub>2</sub> O <sub>4</sub> (1-888),<br>27% CaAl <sub>4</sub> O <sub>7</sub> (23-1037),<br>3% Ca <sub>12</sub> Al <sub>14</sub> O <sub>33</sub> (48-1882),<br>2% $\alpha$ -Al <sub>2</sub> O <sub>3</sub> (1-1243) | Amorphous SiO <sub>2</sub>         | Amorphous SiO <sub>2</sub>       |        |
| Particle size ( $\mu$ m, D <sub>50</sub> /D <sub>90</sub> )  | 1.5/9.6   | 8.0/29                 | 2.0/6.0   | 9 nm/16 nm                         | 11 nm/18 nm                      |        |
| <sup>c</sup> Solid density (g.cm <sup>-3</sup> )             | 3.97  | 3.47                   | 3.23  | 2.10                               | 2.10                             |        |
| <sup>c</sup> Surface area (m <sup>2</sup> .g <sup>-1</sup> ) | 1.3   | 1.5                    | 0.6   | 220                                | 210                              |        |
| <sup>c</sup> Solids content (wt%)                            | -   | -                      | -   | 41.2                               | 39.8                             |        |
| <sup>a</sup> Loss of ignition (wt%)                          | < 0.1   | < 0.1                  | < 0.1   | < 0.1                              | < 0.1                            |        |
| Compositions tested  | CA-MS-CAC   |                        | CA-MS-UCS   |                                    | CA-MS-SCS                        |        |
|  | (wt%)   | (vol%)                 | (wt%)   | (vol%)                             | (wt%)                            | (vol%) |
| CA   | 53.50   | 37.32                  | 56.66   | 38.44                              | 56.66                            | 38.29  |
| MS   | 22.00   | 17.26                  | 22.31   | 17.02                              | 22.31                            | 16.95  |
| CAC  | 11.79   | 10.14                  | -   | -                                  | -                                | -      |
| SiO <sub>2</sub> (from SCS)                                  | -   | -                      | 8.67  | 11.14                              | 8.37                             | 10.72  |
| H <sub>2</sub> O (from SCS)                                  | -   | -                      | 12.37   | 33.40                              | 12.66                            | 34.05  |
| H <sub>2</sub> O   | 12.71   | 35.29                  | -   | -                                  | -                                | -      |
| Dispersant (wt%)   | 0.1   | -                      | 0.1   | -                                  | 0.1                              | -      |
| Total composition (%)  | Mass  | Molar                  | Mass  | Molar                              | Mass                             | Molar  |
| Al <sub>2</sub> O <sub>3</sub>                               | 70.05   | 49.30                  | 64.29   | 44.08                              | 64.51                            | 44.25  |
| MgO  | 25.04   | 44.59                  | 25.25   | 43.79                              | 25.33                            | 43.96  |
| SiO <sub>2</sub>   | 0.72  | 0.86                   | 10.13   | 11.79                              | 9.83                             | 11.44  |
| Na <sub>2</sub> O  | 0.18  | 0.21                   | 0.17  | 0.20                               | 0.18                             | 0.20   |
| Fe <sub>2</sub> O <sub>3</sub>                               | 0.11  | 0.05                   | 0.06  | 0.03                               | 0.06                             | 0.03   |
| CaO  | 3.89  | 4.98                   | 0.10  | 0.13                               | 0.10                             | 0.13   |

<sup>a</sup>After 5 h at 1000°C; <sup>b</sup>As-received raw materials; composition in wt% determined by Rietveld method<sup>25</sup>; <sup>c</sup>After 24 h at 200°C

levels typically attained in the matrixes of refractory castables employed in steelmaking<sup>3,6-8,14,25-28,41,42,49,66,67</sup>.

The initial flowability and setting time were evaluated according to the cone-flow method (adapted from standard ASTM C1437-20, "Standard Test Method for Flow of Hydraulic Cement Mortar"). Non-adherent molds (40 mm diameter  $\times$  60 mm height; 15 molds per composition) were pressed against a flat smooth surface, filled with the suspension, and kept at 60°C (thermal bath, Brookfield TC-550, USA), remaining still. After 5-min intervals, the mold was rapidly lifted so that its content was free to flow, forming a circle. When the free flow stopped, the average diameter of the cycle formed by the suspension (D<sub>f</sub>, mm) was measured and compared with the initial value (D = 40 mm). The process was repeated until there was no significant flow and the free-flowability index (FI, %) was calculated by Equation 3:

$$FFI(\%) = 100\% (D_f - 40) / 40 \quad (3)$$

The workability of the system was evaluated through the time after the end of mixing (t<sub>work</sub>, min) required for the FFI to be reduced to the empirical threshold of 100%. Such time-temperature testing conditions were employed to highlight the extended workability of SCS-containing compositions and because they were employed in previous works for studying the MgO hydroxylation reaction steps<sup>14,15,37,38</sup>.

## 2.2. Samples' preparation and testing

After mixing, equivalent suspensions for each system were cast, respectively, as cylinders of 40 mm length  $\times$  40 mm diameter, for drying and hydroxylation tests; 60 mm length  $\times$  16 mm diameter for total porosity and flexural strength, and measurements; and 8 mm length  $\times$  6 mm diameter for dilatometric analysis.

They remained at  $60^{\circ}\text{C} \pm 1^{\circ}\text{C}$  for 24 h in sealed flasks in an environment of close to 100% relative humidity.

### 2.2.1. Drying and hydroxylation tests

The drying behavior of green humid freshly demolded samples of approximately 100 g was evaluated in tailor-made thermogravimetric equipment capable of supporting cylinders of 40 mm diameter  $\times$  40 mm length<sup>76-78</sup>. It monitors the temperature and mass changes of samples placed in an electric furnace every 10 s. The samples were heated up to  $700^{\circ}\text{C}$  ( $2^{\circ}\text{C}.\text{min}^{-1}$  heating rate) and the instantaneous percent mass loss ( $W$ , wt%) and mass loss rate ( $dW/dT$ , wt%. $^{\circ}\text{C}^{-1}$ ) were calculated by Equations 4 and 5, respectively:

$$W = 100\% \times \left[ \frac{(M_{\text{Inicial}} - M_{\text{Inst}})}{(M_{\text{Inicial}} - M_{\text{Final}})} \right] \quad (4)$$

$$\left( \frac{dW}{dT} \right)_T = \frac{(W_{T+10} - W_{T-10})}{(T_{T+10} - T_{T-10})} \quad (5)$$

where  $M_{\text{Inicial}}$  is the sample's mass after casting and before the curing period,  $M_{\text{Inst}}$  is the instantaneous mass for a certain temperature ( $T$ ), and  $M_{\text{Final}}$  is the mass at the end of heating.

Samples for hydroxylation tests remained in sealed flasks in an environment of relative humidity close to 100% at  $60^{\circ}\text{C}$  for up to 7 days. During the curing period, samples' external dimensions (height,  $H_i$ , and diameter,  $D_i$ , in mm) were continuously measured every 24 h. Equations 6 and 7 provided the external volume ( $V_i$ ) and apparent volumetric expansion (AVE, %). The AVE parameter evaluates the extent of damage inflicted by the hydroxylation expansion upon a ceramic structure and can be continuously measured for a given sample; exponents 0 and E indicate, respectively, the initial stage and condition after a certain hydroxylation period and  $t$  is the thickness of each mold (in mm). A detailed explanation of such techniques and their uses can be found elsewhere<sup>14,37,38,41,42</sup>.

$$V_i = (H_i \times \pi \times (D_i - 2 \times t)^2) / 4 \quad (6)$$

$$\text{AVE} = 100\% \times (V_E - V_0) / V_0 \quad (7)$$

### 2.2.2. Evaluation of physical properties during initial heating towards sintering

For the evaluation of physical properties during initial heating, after the initial period of 24 h at  $60^{\circ}\text{C}$ , samples were demolded and kept in a ventilated environment at  $60^{\circ}\text{C} \pm 1^{\circ}\text{C}$  for 24 h and under vacuum at  $120^{\circ}\text{C} \pm 1^{\circ}\text{C}$  for 24 h. Such curing and drying conditions maximize the binding action of colloidal silica and reduce the risks of damage by MgO excessive hydroxylation and explosive spalling during the first heat-up<sup>37,38,42,79-81</sup>. After drying, samples were thermally treated at  $300\text{--}1600^{\circ}\text{C}$  for 3 h ( $1^{\circ}\text{C}.\text{min}^{-1}$  up to  $400^{\circ}\text{C}$ ,  $1\text{ h}$ ;  $2^{\circ}\text{C}.\text{min}^{-1}$  up to maximum temperature, 3 h hold; cooling rate of  $5^{\circ}\text{C}.\text{min}^{-1}$  up to  $800^{\circ}\text{C}$  and  $10^{\circ}\text{C}.\text{min}^{-1}$  down to room temperature). Those specific temperatures represent important events that can occur during initial heating towards sintering, such as hydrates decomposition, calcium aluminates, and spinel formation<sup>15,81</sup>.

Dried green (G) and sintered (St) samples were measured (length,  $L$ , diameter,  $D$ , in cm) and weighted ( $M$ , g). Their total porosity (TP, %) was calculated by Equations 8, and the solid density ( $\rho$ ) values were determined by Helium pycnometry in equivalent compositions after grinding ( $D_{\text{Particle}} \leq 100\ \mu\text{m}$ ).

$$\text{TP}(\%) = 100\% \times \left\{ 1 - \left[ \frac{(4 \times M)}{\pi \times D^2 \times L \times \rho} \right] \right\} \quad (8)$$

Samples' permanent dimensional thermal linear variation (PV, %) was calculated by Equation 9, whereas dilatometric analyses for dynamic dimensional thermal linear variation (DV, %) were conducted in green dried samples (8 mm length  $\times$  6 mm diameter cylinders; DIL402C, Netzsch, Germany) at a  $5^{\circ}\text{C}.\text{min}^{-1}$  heating rate, up to  $1600^{\circ}\text{C}$ .

$$\text{PV or DV}(\%) = 100 \times \left[ \frac{(L_{St} - L_G)}{L_G} \right] \quad (9)$$

The maximum expansion observed (Maximum dynamic expansion, MDE, and maximum permanent expansion, MPE) and the final dimensional variation after thermal treatment (Final dynamic variation, FDV, and final permanent variation, FPV) were recorded for each dynamic or isothermal treatment test. Such parameters relate the role of colloidal silica and calcium aluminates in the expansive formation of *in situ* spinel and its further sintering behavior, respectively.

Their flexural strength (FS, MPa, Equation 10) was calculated after a three-point bending test in an MTS 810 TestStar II tensile tester, at a  $2\ \text{N}.\text{s}^{-1}$  loading rate:

$$\text{FS}(\text{MPa}) = (8 \times F \times W) / (\pi \times D^3) \quad (10)$$

where  $F$  (in N) is the maximum load before rupture and  $W$  is the support span (40 mm). Each value of total porosity, flexural strength, and apparent volumetric expansion is the average result of the testing of 5 samples and the error bars represent their standard deviation.

The products of hydroxylation tests and sintering thermal treatments were evaluated in equivalent samples regarding crystalline phases' composition (X-ray diffraction, crushed samples,  $D_{\text{Part}} < 100\ \mu\text{m}$ , Rotaflex RV 200B, Rigaku-Denki Corp., Japan,  $\lambda = 0.14506\ \text{nm}$ , in the  $2\theta$  range from  $10$  to  $70^{\circ}$  at a  $0.5^{\circ}.\text{min}^{-1}$  scan rate, against standard JCPDS files; Rietveld method with MATCH! Software, 3.8 version, Germany<sup>75</sup>) and microstructure (scanning electron microscopy, fractured surfaces, FEI 7500F, Netherlands, equipped with an energy dispersive spectrometer, Apollo, EDAX, USA, for elemental composition mapping).

## 3. Results and Discussion

### 3.1. Flowability and workability after mixing

The CAC-bonded suspension (CA-MS-CAC) showed 23 min workability time at  $60^{\circ}\text{C}$ , which is a consistent result in comparison to reference studies that tested similar grade (Figure 2a)<sup>1,2,5,6,7,82-85</sup>. Such long time setting relates to the high amount of water present in the suspension in comparison to a full castable composition containing coarse aggregates<sup>82-85</sup>. As expected, the composition prepared with conventional unsilanized anionic colloidal silica (CA-MS-UCS) showed instantaneous gelling inside the mixing chamber due to the high concentration of  $\text{Mg}^{2+}$  ions (Figure 2b)<sup>86-91</sup>. Conversely, the flowability index levels and workability of the composition containing silanized colloidal silica (CA-MS-SCS) were similar to or higher than those for the CAC-bonded one.

A recent publication explored such unexpected behavior for adding fine MgO sinter particles into aqueous dispersion of silanized colloidal silica<sup>46</sup>. Because of their epoxysilane-modified surfaces, SCS particles are less sensitive to the presence of  $Mg^{2+}$  ions in the suspension and did not gel instantaneously<sup>64-66</sup>. Therefore, during mixing, the cationic surfaces of MgO attracted the anionic SCS particles resulting in a highly negative potential Zeta for over 20 min at 60°C<sup>92,93</sup>. In the present system, since calcined alumina particles are compatible with most anionic grades of colloidal silica (silanized or not)<sup>66,69-71,87,94</sup>, such a favorable combination of effects produced a  $Al_2O_3$ -MgO-SCS-containing suspension that remained fluid for periods longer than 30 min. (Figure 2c).

Because tests conducted with unsilanized anionic colloidal silica dispersion resulted in instantaneous gelling inside the mixing chamber, no reproducible sample of suitable physical integrity could be attained. Consequently, no further tests were carried out with such a composition, and the CAC-containing composition was defined as a reference for the following tests.

### 3.2. Curing and drying behavior

After casting and curing, CAC typically dissolves and reacts with water, precipitating nanometric crystals of calcium aluminate hydrates at the spaces amongst particles<sup>14,42,83,85</sup>, clogging the pores and strengthening the structure<sup>76-78,82,83</sup>.

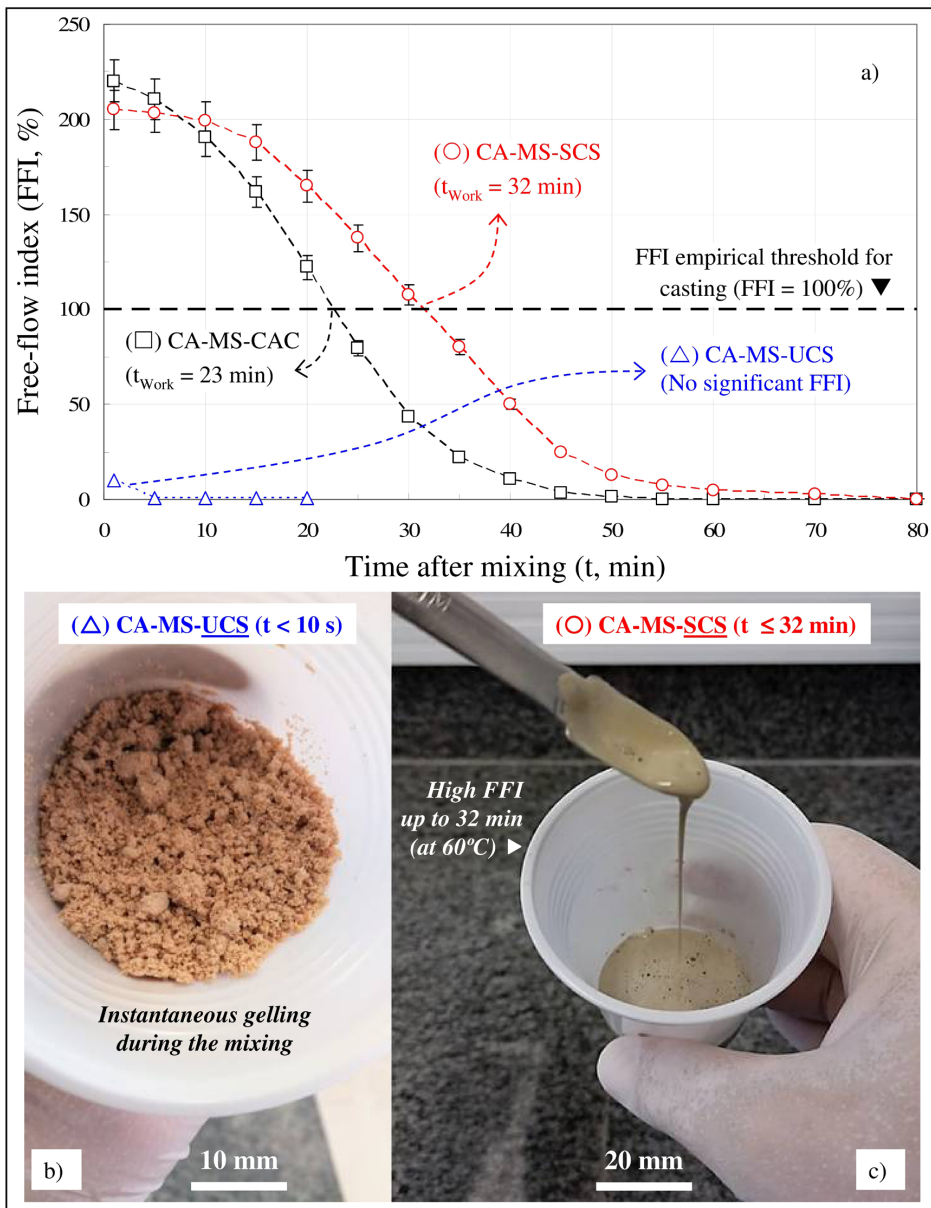


**Figure 2.** a) Free-flow index (FFI) and workability time ( $t_{work}$ ) as a function of time after mixing for compositions containing calcium aluminate cement (CA-MS-CAC), unsilanized colloidal silica (CA-MS-UCS) or silanized colloidal silica (CA-MS-SCS) kept at 60°C for up to 80 min and b) their aspect after mixing (CA-MS-UCS) and c) after up to 32 min after mixing (CA-MS-SCS).

Despite their higher flexural strength (Figure 3), those materials usually show significantly lower permeability and less favorable water withdrawal step in comparison to those bonded with colloidal silica<sup>69-71,74,83,85,94</sup>. In the present study, on the other hand, the opposite drying behavior was observed, i.e., the CAC-bonded sample showed early drying during the curing step (Figure 4a) and its maximum drying rate peak occurred at a temperature lower than the one for the SCS-bonded one (Figure 4b). Such unusual results can be explained through the apparent volumetric expansion measurements (Figure 5) and the crystalline phases identified by XRD (Figures 6a and 7a).

The suspension containing CAC experienced a significant formation of brucite and CAC hydrate katoite ( $C_3AH_6$  or  $Ca_3Al_2(OH)_{12}$ , Figure 6a, corroborated by two intense mass loss rate peaks at approximately 380°C and 430°C, respectively, related to the dehydroxylation of  $Ca_3Al_2(OH)_{12}$  and  $Mg(OH)_2$  (Figure 4b)<sup>14,15,81,83,85</sup>. Previous reports indicated the presence of CAC speeds up and intensifies the hydroxylation reaction of MgO due to the increase in suspensions' pH and inner temperature<sup>14-16</sup>. Moreover, since CAC's hydrates crystals rapidly filled part of the pores of the structure, there was less room to accommodate the extra volume generated during the formation of brucite<sup>14,16,42,44</sup>. Consequently, the first signs of damage by apparent volumetric expansion appeared for the CAC-containing sample after 24-h curing at 60°C. The microcracks formed in the structure during the curing time increased permeability, favored premature water withdrawal ( $W_{0CAC}=15\%$ ), and eased the overall drying during the initial heating. On the other hand, no signs of AVE were detected for the SCS-bonded samples, even after 7-day curing. Besides the very low amount of brucite formed, a talc-based magnesium silicate hydroxide hydrate ( $Mg_5Si_8O_{20}(OH)_2 \cdot 8H_2O$ ) was also identified (Figure 7a)<sup>46,95-98</sup>. Previous studies reported it prevented MgO hydroxylation due to its high stability and insolubility and produce strong bonding connections amongst the particles<sup>41,46,67</sup>. Therefore, the resulting microstructure of the green dried sample comprised a compact mixture of calcined alumina, MgO particles covered with a thin coating of  $Mg_5Si_8O_{20}(OH)_2 \cdot 8H_2O$ , and thicker layers of gelled colloidal silica particles (Figures 8a, b). Although it was dense and crack-free, the drying behavior occurred safely, with no explosive spalling.

### 3.3. Physical properties and microstructure evolution during initial heating

After initial drying at 120°C, CAC-bonded samples showed a significant total porosity increase and strength reduction in the 300-700°C temperature range related to the decomposition of hydroxylated compounds formed during curing (Figure 3)<sup>77,80,81,83-85</sup>. Regarding curing steps conducted above 30°C, Katoite hydrate ( $C_3AH_6$ ) is the main calcium aluminate hydrate formed. Previous studies reported that its decomposition occurs above 350°C and results mainly in  $C_3A$  ( $Ca_3Al_2O_6$ ), CA ( $CaAl_2O_3$ ), and  $C_{12}A_7$  ( $Ca_{12}Al_4O_{33}$ )<sup>83,85</sup>. Due to their higher density in comparison to the hydroxylated state, the formation of such aluminates increased the pore content in the structure concomitantly with the collapse of bridging points amongst particles. Consequently, up to 700°C, the structure became more porous and weaker.

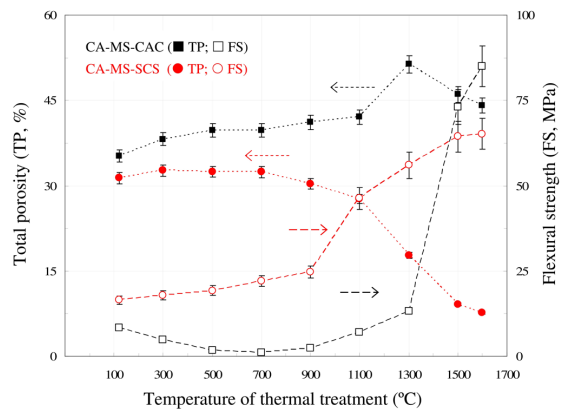


**Figure 3.** Total porosity (TP) and flexural strength (FS) for samples containing calcium aluminate cement (CA-MS-CAC) or silanized colloidal silica after isothermal treatments in the 300-1600°C temperature range for 3 h.

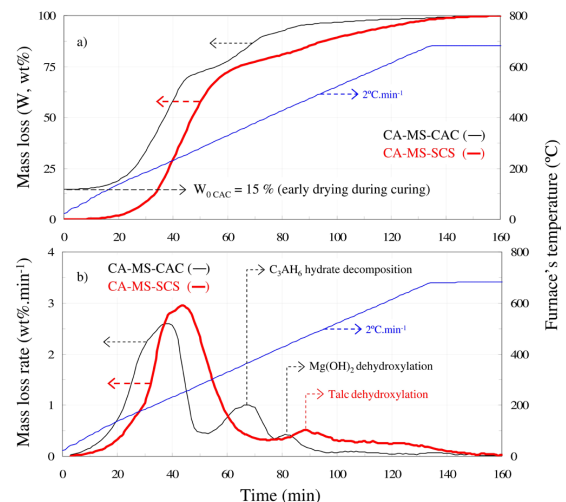


**Figure 4.** Drying behavior (a) mass loss and (b) mass loss rate for freshly demolded samples containing calcium aluminate cement (CA-MS-CAC) or silanized colloidal silica (CA-MS-SCS).

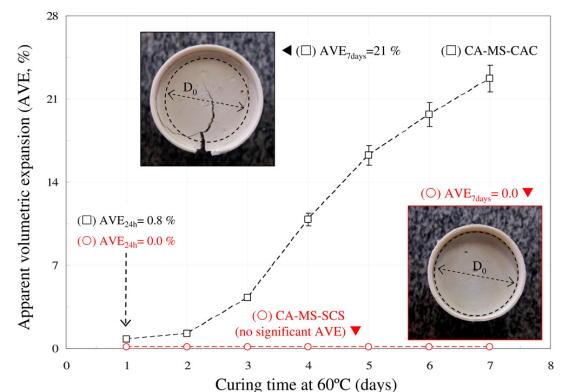


**Figure 5.** Apparent volumetric expansion (AVE) as a function of curing time for samples containing calcium aluminate cement (CA-MS-CAC) or silanized colloidal silica (CA-MS-SCS), for up to 7 days at 60°C. The aspect of the samples after 7 days of testing is also shown.

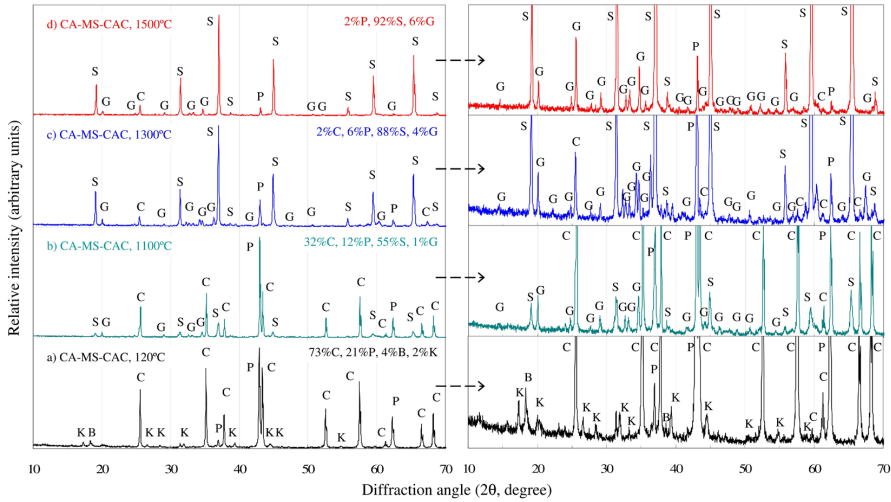


**Figure 6.** X-ray diffraction patterns for CA-MS-CAC composition after a) drying at 120°C overnight and sintering at b) 1100°C, c) 1300°C, and d) 1500°C for 3 h. Graphs on the right represent those on the left at higher magnification. List of symbols: C = Corindon ( $\alpha$ - $\text{Al}_2\text{O}_3$ , PDF = 1-1243), P = Periclase ( $\alpha$ - $\text{MgO}$ , PDF = 1-1235), B = Brucite ( $\text{Mg}(\text{OH})_2$ , PDF = 1-1169), K = Katoite ( $\text{Ca}_3\text{Al}_2(\text{OH})_{12}$  or  $\text{C}_3\text{AH}_6$ , PDF = 24-217), S = Spinel ( $\text{MgAl}_2\text{O}_4$ , PDF = 1-1154), G = Grossite ( $\text{CaAl}_4\text{O}_7$  or  $\text{CA}_2$ , PDF = 23-1037). The numbers on the right indicate the mass percent of each crystalline phase identified.

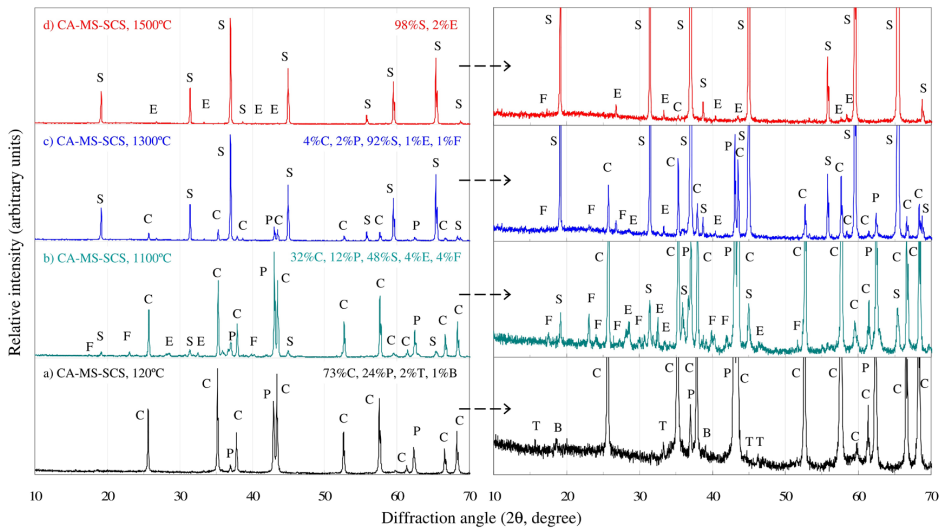


**Figure 7.** X-ray diffraction patterns for CA-MS-SCS composition after a) drying at 120°C overnight and sintering at b) 1100°C, c) 1300°C, and d) 1500°C for 3 h. Graphs on the right represent those on the left at higher magnification. List of symbols: C = Corydon ( $\alpha$ - $\text{Al}_2\text{O}_3$ , PDF = 1-1243), P = Periclase ( $\alpha$ - $\text{MgO}$ , PDF = 1-1235), B = Brucite ( $\text{Mg}(\text{OH})_2$ , PDF = 1-1169), T = Magnesium silicate hydroxide hydrate or Talc ( $\text{Mg}_5\text{Si}_8\text{O}_{20}(\text{OH})_2 \cdot 8\text{H}_2\text{O}$ , PDF = 5-99), S = Spinel ( $\text{MgAl}_2\text{O}_4$ , PDF = 1-1154), F = Forsterite ( $\text{Mg}_2\text{SiO}_4$ , PDF = 1-1290), E = Enstatite ( $\text{MgSiO}_3$ , PDF = 2-546). The numbers on the right indicate the mass percent of each crystalline phase identified.

In this study, the strength reduction was particularly intense due to the microcracks generated during curing and the extra pores formed after  $\text{Mg}(\text{OH})_2$  dehydroxylation<sup>15,42,48,81</sup>. In the 700-900°C range, calcium aluminates begin to merge and rearrange to form single compounds, namely  $\text{CA}_2$  ( $\text{CaAl}_4\text{O}_7$ ), small fractions of  $\text{CA}_6$  ( $\text{CaAl}_{12}\text{O}_{19}$ ), above 1100°C (Figure 6b)<sup>85,99,100</sup>. Above 900°C, the solid-state reaction of magnesium aluminate spinel ( $\text{MgAl}_2\text{O}_4$ ) begins and becomes more intense at approximately 1250°C to consume a significant part of the  $\text{Al}^{3+}$  ions available<sup>19,24,101,102</sup>, favoring the formation

of  $\text{CA}_2$  instead of  $\text{CA}_6$  (Figures 6c, d)<sup>7,8</sup>. Since  $\text{CA}_2$  has lower density and a highly asymmetrical crystalline habit, when its *in situ* formation occurs in the presence of *in situ* spinel, the interlocking of both types of crystals maximizes the expansion of the structure (Figure 9a)<sup>7,8,26</sup>. Although above 1500-1600°C the structure begins to shrink, it also contains unreacted  $\text{MgO}$  and higher than 40% total porosity level (Figure 10). Studies of similar systems reported the challenge of achieving significant levels of densification in high-spinel content structures<sup>4,18-22,30,60,61,63</sup>.

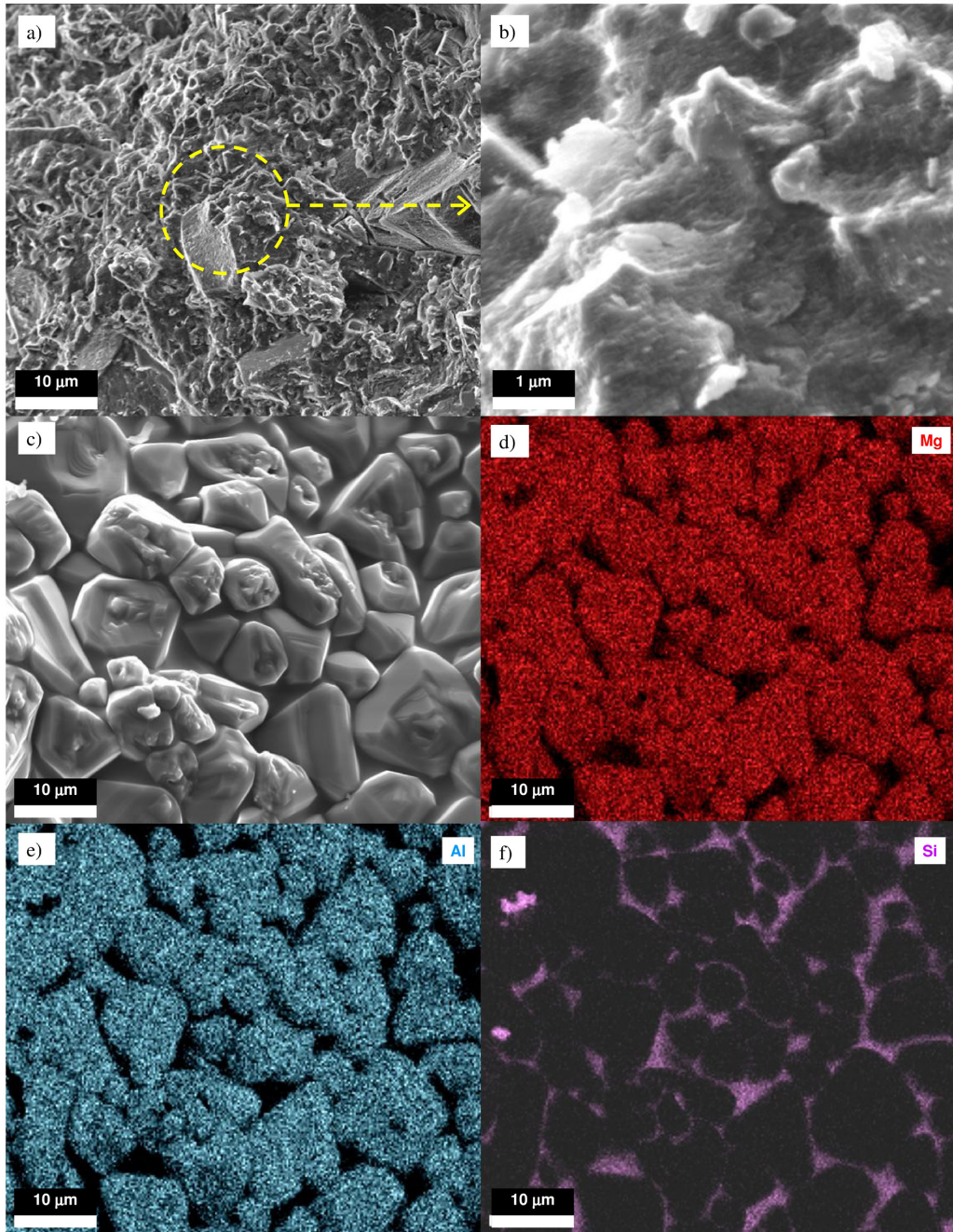


**Figure 8.** SEM images for CA-MS-SCS composition: a-b) green dried at 120°C and c-f) after sintering at 1600°C for 3 h. Elemental analysis: Red for Mg, blue for Al, and pink for Si.

Regarding the SCS-bonded composition, in comparison to its 120°C dried samples, no significant strength reduction occurred after further thermal treatments (Figure 3). Such behavior was observed for other MgO-free systems containing colloidal binders instead of hydraulic ones<sup>2,28,46,66,69-71,89,94,103</sup> and can be attributed to the absence of hydroxylated phases at the bridging points amongst the particles, which do not lose connection during initial heating<sup>46,66,84,85</sup>. At approximately 800°C, the shrinkage event observed can be attributed to the simultaneous decomposition of the magnesium silicate

hydroxide hydrate and softening of the amorphous silica, which promotes a certain degree of accommodation in the structure (Figure 9b)<sup>104-109</sup>. From 900°C up to 1400°C, the expansion event related to spinel formation was less intense than the one observed for CAC-containing compositions, and above this temperature, intense shrinkage and densification occurred. From a technological point of view, those results are highly important regarding the installation, drying, and firing of large monolithic parts that must sustain their weight before sintering<sup>1,2,5,70,73,74,82,83</sup>.

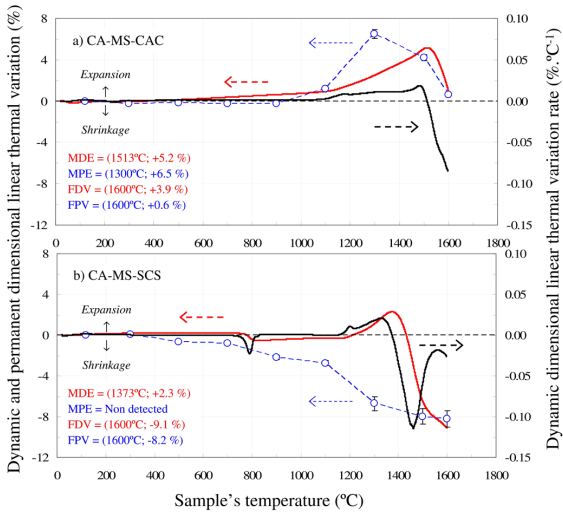


**Figure 9.** Dilatometric analysis of samples containing a) calcium aluminate cement (CA-MS-CAC) or b) silanized colloidal silica during sintering (dynamic dimensional linear thermal variation) or after isothermal treatments in the 300-1600°C temperature range for 3 h (permanent dimensional linear thermal variation). Abbreviations: MDE = maximum dynamic expansion; MPE = maximum permanent expansion; FDV = final dynamic variation; FPV = final permanent variation.

Unlike CAC-containing samples, the SCS-bonded ones showed significant differences between dynamic and permanent dimensional linear thermal variations (Figure 9b). Whereas the dynamic analysis indicated an instantaneous expansive behavior during heating, samples treated under isothermal conditions for longer periods experienced shrinkage at all testing temperatures. Two simultaneous effects explain such a behavior. Firstly, the presence of transient liquids (i.e., compounds of low melting point and viscosity, such as  $C_{12}A_7$ , which melts at around 1360°C) in the CAC-containing samples speeded up the formation of calcium aluminates and spinel [7,25,-28,42,110]. Therefore, reactions conducted under different heating rates behaved similarly. A similar effect was reported by studies that tested CAC-free compositions containing low-purity amorphous silica grades (such as microsilica, which typically contains up to 94-97 wt% of  $SiO_2$ )<sup>27,67,102,103,110</sup>. These works identified significant quantities of the low melting point magnesium aluminum silicates cordierite ( $Mg_2Al_2Si_5O_{18}$ ,  $T_M = 1460^\circ C$ ) and sapphirine ( $Mg_4Al_{10}Si_2O_{23}$ ,  $T_M = 1482^\circ C$ ) besides spinel. On the other hand, high-purity grades of synthetic amorphous silica, such as SCS, show almost no rupture of the silicon-oxygen tetrahedral net by residual alkalis and, due to this, their liquid phase displays very high viscosity and hardly crystallizes above the softening point<sup>79,103-105,109</sup>.

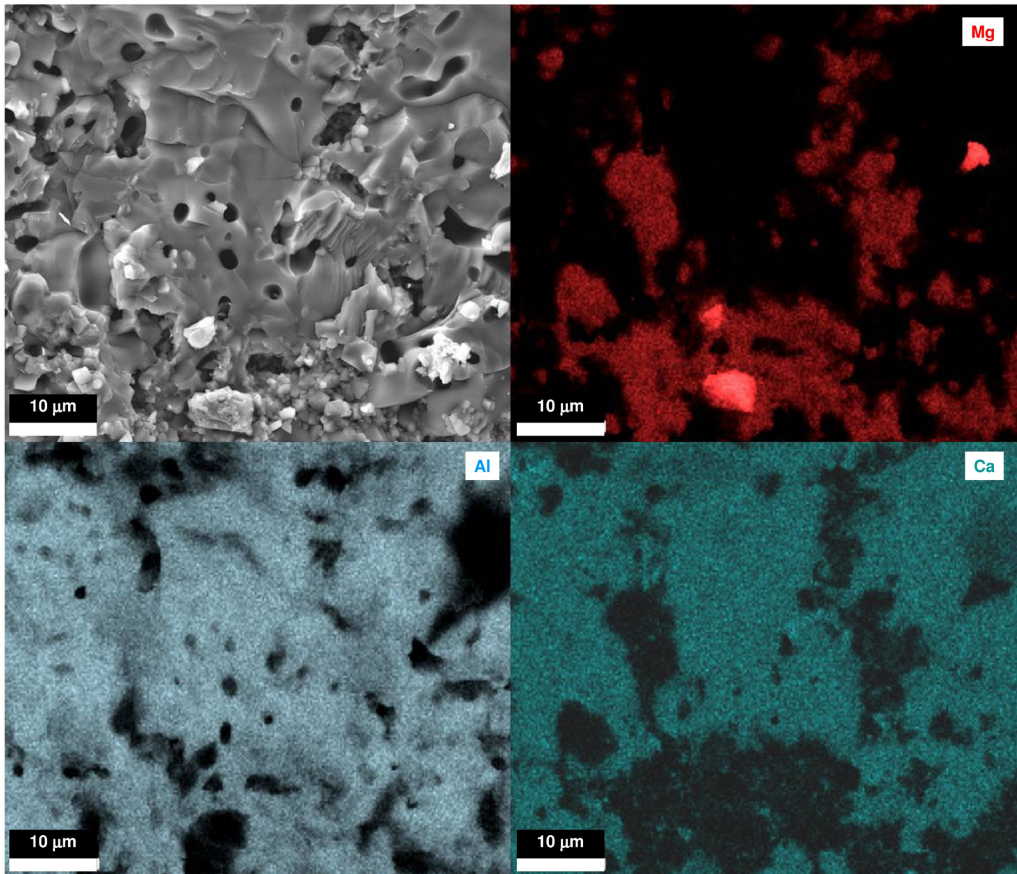


**Figure 10.** SEM images for CA-MS-CAC composition after sintering at 1600°C for 3 h. Elemental analysis: Red for Mg, blue for Al, and green for Ca.

Consequently, it has almost no chemical activity to host permanently  $\text{Al}^{3+}$  and  $\text{Mg}^{2+}$  ions hindering the formation of magnesium-aluminum silicates. Nevertheless, it favored the formation of large faceted spinel crystals and accommodated their expansion, as an indication of the high mobility ions experienced during sintering<sup>3,24,27,50,67,102,110</sup>. The final microstructure attained at 1600°C contains practically no unreacted alumina or MgO and comprises a dense compact of large crystals of spinel surrounded by thin layers of amorphous silica and small portions of magnesium silicate Enstatite ( $\text{MgSiO}_3$ ) pre-formed during the initial heating (Figures 7b-d and 8c-f).

#### 4. Conclusions

The use of silanized colloidal silica (SCS) as a liquid medium and anti-hydroxylation binder for an *in situ* spinel composition comprised of calcined alumina and fine magnesia sinter produced synergistic and technologically useful results. Differently from mixtures of MgO-containing formulations with typical unsilanized anionic colloidal silica, no instantaneous gelling occurred. Conversely, after mixing and homogenization, the suspension attained showed high flowability and workability for periods longer than 30 min at 60°C. After casting and curing, the formation of a protective coating of magnesium silicate hydroxide hydrate ( $\text{Mg}_5\text{Si}_8\text{O}_{20}(\text{OH})_2 \cdot 8\text{H}_2\text{O}$ ) halted the MgO hydroxylation reaction and its deleterious volumetric expansion. No explosive spalling due to pressurized vapor formation occurred during drying tests and high levels of strength were attained in the green-dried state. Unlike the behavior observed for the CAC-bonded reference, the flexural strength of the SCS-containing samples increased continuously due to the total porosity reduction promoted by the thermal treatments towards sintering. The formation of magnesium silicates ( $\text{Mg}_2\text{SiO}_4$  and  $\text{MgSiO}_3$ ) and a remaining portion of non-crystallized amorphous silica favored ions mobility during *in situ* formation of spinel so that its volumetric expansion could be conveniently roomed and large faceted crystals could form and grow. Although further testing of corrosion, creep, and thermal shock resistance is necessary, the high level of densification ( $\text{TP}_{1600^\circ\text{C}} = 7 \pm 0.3\%$ ) and well-built geometry of spinel crystals attained after sintering suggest such a microstructure is Taylor-made for steelmaking applications, such as steel-ladle lining.

#### 5. Acknowledgments

The authors acknowledge Brazilian Research Foundations FAPESP (2010-19274-5; 2017/06738-2; 2018/19773-3; 2022/03655-7), CNPq (305877/2017-8; 304081/2020-5; 150265/2022-0; 311010/2023-7), and CAPES (Finance Code 001) for supporting this research and Almatix (Brazil and USA), ELFUSA Geral de Eletrofusão (Brazil) and Magnesita-RHI (Brazil) for the samples of calcined alumina, calcium aluminate cement, and MgO sinter, respectively. They are indebted to the Electron Microscopy Laboratory of Advanced Materials Research Support Center (SMM/IFSC) for the SEM. They declare that, to the best of their knowledge, no competing interests (financial or personal) affected the results reported in this paper and that they cited all funding and supporting sources.

#### 6. References

- Nishikawa A. Technology of monolithic refractories. Tokyo: Plibrico; 1984. p. 33-7.
- Kataoka M. Unshaped/monolithic in refractories handbook. Tokyo: Technical Association of Refractories of Japan; 1998. p. 230-5.
- Sako EY, Braulio MAL, Pandolfelli VC. The corrosion resistance of microsilica-containing  $\text{Al}_2\text{O}_3$ -MgO and  $\text{Al}_2\text{O}_3$ -spinel castables. Ceram Int. 2012;38(6):4783-9. <http://dx.doi.org/10.1016/j.ceramint.2012.02.066>.
- Ganesh I. A review on magnesium aluminate ( $\text{MgAl}_2\text{O}_4$ ) spinel: synthesis, processing and applications. Int Mater Rev. 2013;58(2):63-112. <http://dx.doi.org/10.1179/1743280412Y.0000000001>.
- Banerjee S. Recent developments in monolithic refractories. Am Ceram Soc Bull. 1998;77(10):59-63.
- Braulio MAL, Bittencourt LRM, Pandolfelli VC. Magnesia grain size effect on in situ spinel refractory castables. J Eur Ceram Soc. 2008;28(15):2845-52. <http://dx.doi.org/10.1016/j.jeurceramsoc.2008.05.014>.
- Braulio MAL, Bittencourt LRM, Pandolfelli VC. Selection of binders for in situ spinel refractory castables. J Eur Ceram Soc. 2009;29(13):2727-35. <http://dx.doi.org/10.1016/j.jeurceramsoc.2009.03.024>.
- Sako EY, Braulio MAL, Zinngrebe E, van der Laan SR, Pandolfelli VC. Fundamentals and applications on in situ spinel formation mechanisms in  $\text{Al}_2\text{O}_3$ -MgO refractory castables. Ceram Int. 2012;38(3):2243-51. <http://dx.doi.org/10.1016/j.ceramint.2011.10.074>.
- Fruhwith O, Herzog GW, Hollerer I, Rchetti A. Dissolution and hydration kinetics of MgO. Surf Technol. 1985;24(3):301-17. [http://dx.doi.org/10.1016/0376-4583\(85\)90080-9](http://dx.doi.org/10.1016/0376-4583(85)90080-9).
- Kitamura A, Onizuka K, Tanaka K. Hydration characteristics of magnesia. Taikabutsu Overseas. 1995;16(3):3-11.
- Kaneyasu A, Yamamoto S, Yoshida A. Magnesia raw materials with improved hydration resistance. Taikabutsu Overseas. 1996;17(2):21-6.
- Birchal VS, Rocha SDF, Mansur MB, Ciminelli VST. A simplified mechanistic analysis of the hydration of magnesia. Can J Chem Eng. 2001;79(4):507-11. <http://dx.doi.org/10.1002/cjce.5450790406>.
- Lee JH, Eun JH, Kim SG, Park SY, Lee MJ, Kim HJ. Hydration behavior of MgO single crystals and thin films. J Mater Res. 2003;18(12):2895-903. <http://dx.doi.org/10.1557/JMR.2003.0404>.
- Salomão R, Bittencourt LRM, Pandolfelli VC. A novel approach for magnesia hydration assessment in refractory castables. Ceram Int. 2007;33(5):803-10. <http://dx.doi.org/10.1016/j.ceramint.2006.01.004>.
- Salomão R, Pandolfelli VC. Magnesia sinter hydration-dehydration behavior in refractory castables. Ceram Int. 2008;34(8):1829-34. <http://dx.doi.org/10.1016/j.ceramint.2007.06.009>.
- Cao F, Miao M, Yan P. Hydration characteristics and expansive mechanism of MgO expansive agents. Constr Build Mater. 2018;183:234-42. <http://dx.doi.org/10.1016/j.conbuildmat.2018.06.164>.
- Alper AM, McNally RN, Ribbe PH, Doman RC. The system MgO-MgAl<sub>2</sub>O<sub>4</sub>. J Am Ceram Soc. 1962;45(6):263-8. <http://dx.doi.org/10.1111/j.1151-2916.1962.tb11141.x>.
- Bayley JT, Russell R. Sintered spinel ceramics. Am Ceram Soc Bull. 1968;47(11):1025-9.
- Bratton RJ. Initial sintering kinetics of  $\text{MgAl}_2\text{O}_4$ . J Am Ceram Soc. 1969;52(8):417-9. <http://dx.doi.org/10.1111/j.1151-2916.1969.tb11971.x>.
- Bayley JT, Russell R. Preparation and properties of dense spinel ceramics in the  $\text{MgAl}_2\text{O}_4$ - $\text{Al}_2\text{O}_3$  system. Br Ceram Soc Trans. 1969;68(4):159-64.
- Bratton RJ. Sintering and grain-growth kinetics of  $\text{MgAl}_2\text{O}_4$ . J Am Ceram Soc. 1971;54(3):141-3. <http://dx.doi.org/10.1111/j.1151-2916.1971.tb12241.x>.

22. Bayley JT, Russell R. Magnesia-rich  $MgAl_2O_4$  spinel ceramics. *Am Ceram Soc Bull.* 1971;50(5):493-6.
23. Sickafus KE, Wills JM, Grimes NW. Structure of spinel. *J Am Ceram Soc.* 1999;82(12):3279-92. <http://dx.doi.org/10.1111/j.1151-2916.1999.tb02241.x>.
24. Watson EB, Price JD. Kinetics of the reaction  $MgO+Al_2O_3 \rightarrow MgAl_2O_4$  and Al-Mg interdiffusion in spinel at 1200 to 2000°C and 1.0 to 4.0 GPa. *Geochim Cosmochim Acta.* 2002;66(12):2123-38. [http://dx.doi.org/10.1016/S0016-7037\(02\)00827-X](http://dx.doi.org/10.1016/S0016-7037(02)00827-X).
25. Braulio MAL, Castro JFR, Pagliosa C, Bittencourt LRM, Pandolfelli VC. From macro to nanomagnesia: designing the in situ spinel expansion. *J Am Ceram Soc.* 2008;91(9):3090-3. <http://dx.doi.org/10.1111/j.1151-2916.2008.02566.x>.
26. Braulio MAL, Bittencourt LRM, Pandolfelli VC. Magnesia grain size effect on in situ spinel refractory castables. *J Eur Ceram Soc.* 2008;28(15):2845-52. <http://dx.doi.org/10.1016/j.jeurceramsoc.2008.05.014>.
27. Braulio MAL, Brant POC, Bittencourt LRM, Pandolfelli VC. Microsilica or MgO grain size: which one mostly affects the in situ spinel refractory castable expansion? *Ceram Int.* 2009;35(8):3327-34. <http://dx.doi.org/10.1016/j.ceramint.2009.05.031>.
28. Braulio MAL, Piva MFL, Silva E, Pandolfelli VC. *in situ* spinel expansion design by colloidal alumina suspension addition. *J Am Ceram Soc.* 2009;92(2):559-62. <http://dx.doi.org/10.1111/j.1151-2916.2009.02934.x>.
29. Tripathi HS, Ghosh A. Spinelisation and properties of  $Al_2O_3$ - $MgAl_2O_4$ -C refractory: effect of MgO and  $Al_2O_3$  reactants. *Ceram Int.* 2010;36(4):1189-92. <http://dx.doi.org/10.1016/j.ceramint.2009.12.011>.
30. Salomão R, Arruda CC, Pandolfelli VC, Fernandes L. Designing high-temperature thermal insulators based on densification-resistant in situ porous spinel. *J Eur Ceram Soc.* 2021;41(4):2923-37. <http://dx.doi.org/10.1016/j.jeurceramsoc.2020.12.014>.
31. Láská M, Valtýni J, Fellner P. Influence of pH on the crystal size distribution of  $Mg(OH)_2$  prepared by the hydration of MgO. *Cryst Res Technol.* 1993;28(7):931-6. <http://dx.doi.org/10.1002/crat.2170280709>.
32. Gao, P.-W., Wu, S.-X., Lin, P.-H., Wu, Z.-R., Tang, M.-S. Morphology of MgO hydration products under different curing conditions. *Chin J Inorg Chem.* 2007;23(6):1063-8.
33. Aphane ME, van der Merwe EM, Strydom CA. Influence of hydration time on the hydration of MgO in water and in a magnesium acetate solution. *J Therm Anal Calorim.* 2009;96(3):987-92. <http://dx.doi.org/10.1007/s10973-008-9095-y>.
34. Birchal VSS, Rocha SDF, Ciminnelli VST. Effect of magnesite calcination conditions on magnesia hydration. *Miner Eng.* 2000;13(14-15):1629-33. [http://dx.doi.org/10.1016/S0892-6875\(00\)00146-1](http://dx.doi.org/10.1016/S0892-6875(00)00146-1).
35. Chen S, Chen G, Cheng J, Tian F. Effect of additives on the hydration resistance of materials synthesized from the magnesia-calcia system. *J Am Ceram Soc.* 2000;83(7):1810-2. <http://dx.doi.org/10.1111/j.1151-2916.2000.tb01469.x>.
36. Rocha SDF, Mansur MB, Ciminnelli VST. Kinetics and mechanistic analysis of caustic magnesia hydration. *J Chem Technol Biotechnol.* 2004;79(8):816-21. <http://dx.doi.org/10.1002/jctb.1038>.
37. Salomão R, Arruda CC, Souza ADV, Fernandes L. Novel insights into MgO hydroxylation: effects of testing temperature, samples' volume and solid load. *Ceram Int.* 2014;40(9, Suppl 9 Pt. B):14809-15. <http://dx.doi.org/10.1016/j.ceramint.2014.06.074>.
38. Salomão R, Arruda CC, Kawamura MA. A systemic investigation on the hydroxylation behavior of caustic magnesia and magnesia sinter. *Ceram Int.* 2015;41(10):13998-4007. <http://dx.doi.org/10.1016/j.ceramint.2015.07.012>.
39. Filippou D, Katiforis N, Papassiopi N, Adam K. On the kinetics of magnesia hydration in magnesium acetate solutions. *J Chem Technol Biotechnol.* 1999;74(4):322-8. [http://dx.doi.org/10.1002/\(SICI\)1097-4660\(199904\)74:4<322::AID-JCTB35>3.0.CO;2-L](http://dx.doi.org/10.1002/(SICI)1097-4660(199904)74:4<322::AID-JCTB35>3.0.CO;2-L).
40. Ghanbari Ahari K, Sharp JH, Lee WE. Hydration of refractory oxides in castable bond systems-II: alumina-silica and magnesia-silica mixtures. *J Eur Ceram Soc.* 2003;23(16):3071-7. [http://dx.doi.org/10.1016/S0955-2219\(03\)00115-8](http://dx.doi.org/10.1016/S0955-2219(03)00115-8).
41. Salomão R, Pandolfelli VC. Microsilica addition as an antihydration technique for magnesia-containing refractory castables. *Am Ceram Soc Bull.* 2007;86(6):9301-9.
42. Salomão R, Pandolfelli VC. The role of hydraulic binders on magnesia containing refractory castables: calcium aluminate cement and hydratable alumina. *Ceram Int.* 2009;35(8):3117-24. <http://dx.doi.org/10.1016/j.ceramint.2009.04.023>.
43. Salomão R, Pandolfelli VC. Citric acid as anti-hydration additive for magnesia containing refractory castables. *Ceram Int.* 2011;37(6):1839-42. <http://dx.doi.org/10.1016/j.ceramint.2011.03.050>.
44. dos Santos T Jr, dos Santos J, Luz AP, Pagliosa C, Pandolfelli VC. Kinetic control of MgO hydration in refractory castables by using carboxylic acids. *J Eur Ceram Soc.* 2018;38(4):2152-63. <http://dx.doi.org/10.1016/j.jeurceramsoc.2017.11.046>.
45. Fini DS, Miguel VC, Pinto VS, Pandolfelli VC, Moreira MH, Luz AP. Aluminum lactate role in improving hydration and drying behavior of MgO-bonded refractory castables. *Ceram Int.* 2020;46(10):17093-102. <http://dx.doi.org/10.1016/j.ceramint.2020.04.006>.
46. Salomão R, Martinatti IS, Fernandes L, Sundblom A, Greenwood P, Tiba PRT. Novel silanized colloidal silica-MgO self-flowing dispersions with improved hydroxylation resistance. *J Eur Ceram Soc.* 2023;43(13):5691-705. <http://dx.doi.org/10.1016/j.jeurceramsoc.2023.05.023>.
47. Ali MM, Mullick AK. Volume stabilization of high MgO cement: effect of curing conditions and fly ash addition. *Cement Concr Res.* 1998;28(11):1585-94. [http://dx.doi.org/10.1016/S0008-8846\(98\)00140-9](http://dx.doi.org/10.1016/S0008-8846(98)00140-9).
48. Salomão R, Bittencourt LRM, Pandolfelli VC. A novel magnesia based binder (MBB) for refractory castables. *Int Ceram Rev.* 2009;58(4):21-4.
49. Sako EY, Braulio MAL, Pandolfelli VC. How effective is the addition of nanoscaled particles to alumina-magnesia refractory castables? *Ceram Int.* 2012;38(6):5157-64. <http://dx.doi.org/10.1016/j.ceramint.2012.03.021>.
50. Jayaseelan DD, Zhang S, Hashimoto S, Lee WE. Template formation of magnesium aluminate ( $MgAl_2O_4$ ) spinel microplatelets in molten salt. *J Eur Ceram Soc.* 2007;27(16):4745-9. <http://dx.doi.org/10.1016/j.jeurceramsoc.2007.03.027>.
51. Gusmano G, Nunziante P, Traversa E, Chiozzini G. The mechanism of  $MgAl_2O_4$  spinel formation from the thermal decomposition of coprecipitated hydroxides. *J Eur Ceram Soc.* 1991;7(1):31-9. [http://dx.doi.org/10.1016/0955-2219\(91\)90051-Z](http://dx.doi.org/10.1016/0955-2219(91)90051-Z).
52. Wang CT, Lin LS, Yang SJ. Preparation of  $MgAl_2O_4$  spinel powders via freeze-drying of alkoxide precursors. *J Am Ceram Soc.* 1992;75(8):2240-3. <http://dx.doi.org/10.1111/j.1151-2916.1992.tb04490.x>.
53. Montouillout V, Massiot D, Douy A, Coutures JP. Characterization of  $MgAl_2O_4$  precursor powders prepared by aqueous route. *J Am Ceram Soc.* 1999;82(12):3299-304. <http://dx.doi.org/10.1111/j.1151-2916.1999.tb02243.x>.
54. Shiono T, Shiono K, Miyamoto K, Pezzotti G. Synthesis and characterization of  $MgAl_2O_4$  spinel precursor from a heterogeneous alkoxide solution containing fine MgO powder. *J Am Ceram Soc.* 2000;83(1):235-7. <http://dx.doi.org/10.1111/j.1151-2916.2000.tb01180.x>.
55. Ganesh I, Srinivas B, Johnson R, Saha BP, Mahajan YR. Microwave assisted solid state reaction synthesis of  $MgAl_2O_4$  spinel powders. *J Eur Ceram Soc.* 2004;24(2):201-7. [http://dx.doi.org/10.1016/S0955-2219\(03\)00602-2](http://dx.doi.org/10.1016/S0955-2219(03)00602-2).
56. Naskar MK, Chatterjee M. Magnesium aluminate ( $MgAl_2O_4$ ) spinel powders from water-based sols. *J Am Ceram Soc.* 2005;88(1):38-44. <http://dx.doi.org/10.1111/j.1151-2916.2004.00019.x>.

57. Zawrah MF, Hamaad H, Meky S. Synthesis and characterization of nano  $MgAl_2O_4$  spinel by the co-precipitated method. *Ceram Int.* 2007;33(6):969-78. <http://dx.doi.org/10.1016/j.ceramint.2006.02.015>.
58. Păcurariu C, Lazău I, Ecsedi Z, Lazău R, Barvinschi P, Mărginean G. New synthesis methods of  $MgAl_2O_4$  spinel. *J Eur Ceram Soc.* 2007;27(2-3):707-10. <http://dx.doi.org/10.1016/j.jeurceramsoc.2006.04.050>.
59. Ianoş R, Lazău I, Păcurariu C, Barvinschi P. Solution combustion synthesis of  $MgAl_2O_4$  using fuel mixtures. *Mater Res Bull.* 2008;43(12):3408-15. <http://dx.doi.org/10.1016/j.materresbull.2008.02.003>.
60. Ianoş R, Lazău R. Combustion synthesis, characterization and sintering behavior of magnesium aluminate ( $MgAl_2O_4$ ) powders. *Mater Chem Phys.* 2009;115(2-3):645-8. <http://dx.doi.org/10.1016/j.matchemphys.2009.01.028>.
61. Esposito L, Piancastelli A, Martelli S. Production and characterization of transparent  $MgAl_2O_4$  prepared by hot pressing. *J Eur Ceram Soc.* 2013;33(4):737-47. <http://dx.doi.org/10.1016/j.jeurceramsoc.2012.10.013>.
62. Prabhakaran K, Patil DS, Dayal R, Gokhale NM, Sharma SC. Synthesis of nanocrystalline magnesium aluminate ( $MgAl_2O_4$ ) spinel powder by the urea-formaldehyde polymer gel combustion route. *Mater Res Bull.* 2009;44(3):613-8. <http://dx.doi.org/10.1016/j.materresbull.2008.06.029>.
63. Zhang P, Liu P, Sun Y, Wang J, Wang Z, Wang S, et al. Aqueous gelcasting of the transparent  $MgAl_2O_4$  spinel ceramics. *J Alloys Compd.* 2015;646:833-6. <http://dx.doi.org/10.1016/j.jallcom.2015.05.275>.
64. Otterstedt JE, Greenwood P. Some important, fairly new uses of colloidal silica/silica sol. In: Bergna HE, Roberts WO, editors. *Colloidal silica: fundamentals and applications*. Boca Raton: Taylor & Francis; 2005. p. 737-56.
65. Greenwood P, Gevert B. Aqueous silane modified silica sols: theory and preparation. *Pigm Resin Technol.* 2011;40(5):275-84. <http://dx.doi.org/10.1108/03699421111176171>.
66. Wang L, Liang Y, Yin Y, Zhao L, Cai M, Nie J. Enhancing the green mechanical strength of colloidal silica-bonded alumina castables using a silane coupling agent. *Ceram Int.* 2016;42(9):11496-9. <http://dx.doi.org/10.1016/j.ceramint.2016.04.045>.
67. Myhre B, Sandberg B, Hundere AM. Castables with  $MgO-SiO_2-Al_2O_3$  as bond phase. In: XXVI ALAFAR Congress; 1997; San Juan, Puerto Rico. Proceedings. Norway: Elkem Materials; 1997.
68. Chakrabarti BK. Drying conditions and their effect on ceramic shell investment casting process. *Mater Sci Technol.* 2002;18(8):935-40. <http://dx.doi.org/10.1179/026708302225004775>.
69. Ismael MR, Salomão R, Pandolfelli VC. Optimization of the particle size distribution of colloidal silica containing refractory castables. *Int Ceram Rev.* 2007;56(4):34-9.
70. Ismael MR, Salomão R, Pandolfelli VC. Refractory castables based on colloidal silica and hydratable alumina. *Am Ceram Soc Bull.* 2007;86(9):58-61.
71. Souri AR, Mirhadi B, Kashani Nia F. The effect of nano-structured colloidal silica on the properties of tabular alumina castables. *Int Ceram Rev.* 2008;57(6):414-6.
72. Salomão R, Souza ADM, Fernandes L, Arruda CC. Advances in nanotechnology for refractories: when very small meets hot, heavy, and large. *Am Ceram Soc Bull.* 2013;92(7):22-7.
73. Sarkar R. Nanotechnology in refractory castables: an overview. *Int Ceram Rev.* 2018;67(S1):22-31. <http://dx.doi.org/10.1007/s42411-018-0039-7>.
74. Roy J, Chandra S, Maitra S. Nanotechnology in castable refractory. *Ceram Int.* 2019;45(1):19-29. <http://dx.doi.org/10.1016/j.ceramint.2018.09.261>.
75. McCusker LB, Von Dreele RB, Cox DE, Louër D, Scardi P. Rietveld refinement guidelines. *J Appl Cryst.* 1999;32(1):36-50. <http://dx.doi.org/10.1107/S0021889898009856>.
76. Innocentini MDM, Salomão R, Ribeiro C, Cardoso FA, Pandolfelli VC, Rettore RP, et al. Permeability of fiber-containing refractory castables. *Am Ceram Soc Bull.* 2002;81(8):65-8.
77. Innocentini MDM, Ribeiro C, Salomão R, Pandolfelli VC, Bittencourt LRM. Assessment of mass loss and permeability changes during the dewatering process of refractory castables containing polypropylene fibers. *J Am Ceram Soc.* 2002;85(8):2110-2. <http://dx.doi.org/10.1111/j.1151-2916.2002.tb00413.x>.
78. Salomão R, Cardoso FA, Bittencourt LRM. Effect of polymeric fibers on refractory castable permeability. *Am Ceram Soc Bull.* 2003;82(4):51-6.
79. Sousa LL, Souza ADV, Fernandes L, Arantes VL, Salomão R. Development of densification-resistant castable porous structures from in situ mullite. *Ceram Int.* 2015;41(8):9443-54. <http://dx.doi.org/10.1016/j.ceramint.2015.03.328>.
80. Souza ADV, Salomão R. Evaluation of the porogenic behavior of aluminum hydroxide particles of different size distributions in castable high-alumina structures. *J Eur Ceram Soc.* 2016;36(3):885-97. <http://dx.doi.org/10.1016/j.jeurceramsoc.2015.11.019>.
81. Salomão R, Arruda CC, Antunes MLP. Synthesis, dehydroxylation and sintering of porous  $Mg(OH)_2-MgO$  clusters: evolution of microstructure and physical properties. *Int Ceram Rev.* 2020;69(1):52-62. <http://dx.doi.org/10.1007/s42411-019-0067-y>.
82. Oliveira IR, Salomão R, Pandolfelli VC, Studart AR. High-carbon-content refractory castables. *Am Ceram Soc Bull.* 2003;82(10):9501-8.
83. Salomão R, Ismael MR, Pandolfelli VC. Hydraulic binders for refractory castables: mixing, curing and drying. *CFI Ceram Forum Int.* 2007;84(9):E103-8.
84. Salomão R, Kawamura MA, Souza ADV, Sakihama J. Hydratable alumina-bonded suspensions: evolution of microstructure and physical properties during first heating. *Int Ceram Rev.* 2017;66(7):28-37. <http://dx.doi.org/10.1007/BF03401226>.
85. Salomão R, Kawamura MA, Emilio ABV, Sakihama J, Segadães AM. Calcium aluminate cement in castable alumina: from hydrate bonding to the in situ formation of calcium hexaluminate. *Ceram Int.* 2021;47(11):15082-93. <http://dx.doi.org/10.1016/j.ceramint.2021.02.066>.
86. Iler RK. Coagulation of colloidal silica by calcium ions, mechanism, and effect of particle size. *J Colloid Interface Sci.* 1975;53(3):476-88. [http://dx.doi.org/10.1016/0021-9797\(75\)90065-X](http://dx.doi.org/10.1016/0021-9797(75)90065-X).
87. Bigley C, Greenwood P. Using silica to control bleed and segregation in self-compacting concrete. *Concrete.* 2003;37(2):43-5.
88. Anjos RD, Ismael MR, Oliveira IR, Pandolfelli VC. Workability and setting parameters evaluation of colloidal silica bonded refractory suspensions. *Ceram Int.* 2008;34(1):165-71. <http://dx.doi.org/10.1016/j.ceramint.2006.09.004>.
89. Hamedani Golshan N, Sarpooolaky H, Souri AR. Microstructure and properties of colloidal silica bonded magnesite castable refractories. *Iran J Mater Sci Eng.* 2011;8(1):25-31.
90. Cai M, Liang Y, Yin Y, Nie J. Effect of citric acid on the hydration process of colloidal silica-bonded magnesia gunning materials. *Ceram Int.* 2019;45(12):15514-9. <http://dx.doi.org/10.1016/j.ceramint.2019.05.055>.
91. Cai M, Liang Y, Nie J, Yin Y, Ju M, Zhang Q. Colloidal silica-bonded  $MgO-CaO$  hot gunning mixes: characterization of physical properties, microstructure and gunning performance. *Ceram Int.* 2019;45(17):22426-31. <http://dx.doi.org/10.1016/j.ceramint.2019.07.232>.
92. Johnson A-CJH, Greenwood P, Hagström M, Abbas Z, Wall S. Aggregation of nanosized colloidal silica in the presence of various alkali cations investigated by the electrospray technique. *Langmuir.* 2008;24(22):12798-806. <http://dx.doi.org/10.1021/la8026122>.
93. Fu L, Ybert C, Bonhomme O, Joly L, Biance A-L. Electrokinetic sweeping of colloids at a reactive magnesium oxide interface. *Soft Matter.* 2021;17(38):8705-11. <http://dx.doi.org/10.1039/D1SM00908G>.

94. Burgos-Montes O, Álvarez M, Aza AH, Pena P, Baudin C. The main role of silica: based cement free binders on the microstructural evolution and mechanical behaviour of high alumina castables. *J Eur Ceram Soc.* 2018;38(11):4137-48. <http://dx.doi.org/10.1016/j.jeurceramsoc.2018.04.048>.
95. Temuujin J, Okada K, MacKenzie KJD. Role of water in the mechanochemical reactions of MgO-SiO<sub>2</sub> systems. *J Solid State Chem.* 1998;138(1):169-77. <http://dx.doi.org/10.1006/jssc.1998.7768>.
96. Temuujin J, Okada K, MacKenzie KJD. Formation of layered magnesium silicate during the aging of magnesium hydroxide-silica mixtures. *J Am Ceram Soc.* 1998;81(3):754-6. <http://dx.doi.org/10.1111/j.1151-2916.1998.tb02405.x>.
97. Li Z, Zhang T, Hu J, Tang Y, Niu Y, Wei J, et al. Characterization of reaction products and reaction process of MgO-SiO<sub>2</sub>-H<sub>2</sub>O system at room temperature. *Constr Build Mater.* 2014;61:252-9. <http://dx.doi.org/10.1016/j.conbuildmat.2014.03.004>.
98. Nied D, Enemark-Rasmussen K, L'Hopital E, Skibsted J, Lothenbach B. Properties of magnesium silicate hydrates (M-S-H). *Cement Concr Res.* 2016;79:323-32. <http://dx.doi.org/10.1016/j.cemconres.2015.10.003>.
99. Oliveira IR, Leite VMC, Lima MPVP, Salomão R. Production of porous ceramic material using different sources of alumina and calcia. *Materia.* 2015;20(3):739-46. <http://dx.doi.org/10.1590/S1517-707620150003.0078>.
100. Costa LMM, Sakihama J, Salomão R. Characterization of porous calcium hexaluminate ceramics produced from calcined alumina and microspheres of Vaterite ( $\mu$ -CaCO<sub>3</sub>). *J Eur Ceram Soc.* 2018;38(15):5208-18. <http://dx.doi.org/10.1016/j.jeurceramsoc.2018.07.034>.
101. Li DX, Pirouz P, Heuer AH, Yadavalli S, Flynn CP. A high-resolution electron microscopy study of MgO/Al<sub>2</sub>O<sub>3</sub> interfaces and MgAl<sub>2</sub>O<sub>4</sub> spinel formation. *Philos Mag A Phys Condens Matter Defects Mech Prop.* 1992;65(2):403-25. <http://dx.doi.org/10.1080/01418619208201530>.
102. Park HC, Lee YB, Oh KD, Riley FL. Grain growth in sintered MgAl<sub>2</sub>O<sub>4</sub> spinel. *J Mater Sci Lett.* 1997;16(22):1841-4. <http://dx.doi.org/10.1023/A:1018585105949>.
103. Salomão R, Fernandes L, Spera NCM. Combined effects of SiO<sub>2</sub> ratio and purity on physical properties and microstructure of in situ alumina-mullite ceramic. *Int J Appl Ceram Technol.* 2021;18(5):1702-9. <http://dx.doi.org/10.1111/ijac.13733>.
104. Iler RK. The chemistry of silica: solubility, polymerization, colloid and surface properties. 1st ed. New York: John Wiley & Sons; 1979. p. 40-9, 161-3, 180-5, 364-6, 624-37.
105. Vansant EF, van der Voort P, Vrancken KC. The surface chemistry of silica. *Stud Surf Sci Catal.* 1995;93:59-77. [http://dx.doi.org/10.1016/S0167-2991\(06\)81511-9](http://dx.doi.org/10.1016/S0167-2991(06)81511-9).
106. Lanás J, Alvarez JI. Dolomitic lime: thermal decomposition of nesquehonite. *Thermochim Acta.* 2004;421(1-2):123-32. <http://dx.doi.org/10.1016/j.tca.2004.04.007>.
107. Jin F, Al-Tabbaa A. Thermogravimetric study on the hydration of reactive magnesia and silica mixture at room temperature. *Thermochim Acta.* 2013;566:162-8. <http://dx.doi.org/10.1016/j.tca.2013.05.036>.
108. Salomão R, Fernandes L. Porous co-continuous mullite structures obtained from sintered aluminum hydroxide and synthetic amorphous silica. *J Eur Ceram Soc.* 2017;37(8):2849-56. <http://dx.doi.org/10.1016/j.jeurceramsoc.2017.03.017>.
109. Fernandes L, Salomão R. Preparation and characterization of mullite-alumina structures formed "in situ" from calcined alumina and different grades of synthetic amorphous silica. *Mater Res.* 2018;21(3):e20170783. <http://dx.doi.org/10.1590/1980-5373-mr-2017-0783>.
110. Jung I-H, Deckerov SA, Pelton AD. Critical thermodynamic evaluation and optimization of the MgO-Al<sub>2</sub>O<sub>3</sub>, CaO-MgO-Al<sub>2</sub>O<sub>3</sub>, and MgO-Al<sub>2</sub>O<sub>3</sub>-SiO<sub>2</sub> systems. *J Phase Equilibria Diffus.* 2004;25(4):329-45. <http://dx.doi.org/10.1007/s11669-004-0151-4>.